MOLECULAR STRUCTURE AND DYNAMICS OF A NONIONIC SURFACTANT ($C_{12}E_5$) IN LAMELLAR PHASE:

^{13}C Solid State NMR and MD Simulations

Master project thesis

Author:
Roberta Pigliapochi

Supervisor:
Daniel Topgaard

Assistant Supervisors:
Tiago Ferreira
Samuli Ollila

Contents

Chapter 1

Introduction

Lipids and surfactants are amphiphilic molecules that, in acqueous solution, aggregate in particular self-assembly structures depending on both their chemical properties and external conditions [1].

The nature of the motion processes occurring in these systems is various and spread on a wide range of characteristic time scales [2, 3, 4, 5]: aside from the very fast dynamics regarding motions of the chain itself, as bond bending, trans-gauche isomerization and fast molecular rotation, that can be overall described in a time range between ps and hundreds of ns, by broadening the view to the whole assemblied system other slower mechanisms take place, as molecular exchange between domain with different orientations, and flip-flop transition, covering a time range that goes from μs up to s. Thus, the analysis of the dynamics of the system and an overview to the mechanisms taking place at the molecular level get difficult to obtain. Nuclear Magnetic Resonance relaxation studies on molecular dynamics are frequently investigated [6, 7, 8, 9, 10, 11] due to their efficiency and specificity. For simple systems of molecules in solution or at solid state, the correlation time, τ, and the order parameter, S, which are respectively expression of the rate of the motions and the spatial restriction of the different sites and which modulate the relaxation mechanisms in analysis, can be fairly estimated [6, 12, 13]. Nevertheless, the information concerning the nature of the internal motions obtained through NMR data on assemblied surfactant lamellar phase is more tricky to be depicted because of the spread variety of the dynamics involving the observable sites [14].

In the following work, a theoretical framework for interpreting nuclear magnetic resonance relaxation, already presented in regards to macromolecules [15], is improved in order to achieve a deeper insight of the dynamics of surfactants in lamellar phase.

In particular, the attention focuses on the study of the correlation function $g(\tau)$ describing the motion of each C-H bond through the average

$$g(\tau) = \langle P_2[\vec{\mu}(t+\tau) \cdot \vec{\mu}(t)] \rangle_t, \tag{1.1}$$

with P_2 representing the second Legendre polynomial and $\vec{\mu}(\tau)$ being the unitary vector in the direction of the bond. The presented specific espression of $g(\tau)$ in regards to a lamellar phase leads to the definition of the effective correlation time, τ_e, direct measure of the time scale of the motions of these systems at high frequencies.

Chapter 2

Theory and Concepts

2.1 Nuclear Spin Relaxation

Many motional mechanisms in molecules can be studied by nuclear spin relaxation [16, 17]. This process in a system of ^{13}C-^{1}H nuclear pairs is caused by fluctuating magnetic fields at the sites of the nuclear spins [18]: these fluctuations are due to, for instance, direct dipole-dipole coupling between two spins, that changes the effective magnetic field felt by the nuclei as motions and tumblings occur. Another source of fluctuations arises as an effect of the Chemical Shift Anisotropy (CSA) [19]: the non-spherical but rather ellipsoidal symmetry of the electron cloud around the nucleus makes the net magnetic field felt by the spins dependent on its orientation.

The presence of these interactions affecting the spin relaxation is related with the isotropy or anisotropy of the system. An analysis of the orientation dependence [20] can be obtained by defining the order parameter, S_{CH}, specific for each C-H bond and of the form

$$S_{CH} = \frac{1}{2}\langle 3\cos^2\theta - 1\rangle. \tag{2.1}$$

The orientation order parameter, S_{CH}, is an average over time and space depending on θ, the angle between the external magnetic field and the axis of each C-H bond. In isotropic systems, due to their directionally indipendence, the C-H bonds are characterised by S_{CH}=0, leading to an averaging out of the dipolar coupling and CSA effects.

On the contrary, anisotropic systems, as surfactants in lamellar phase, are characterised by S_{CH} not equal to zero: as a consequence, dipolar and CSA interactions are not averaged out as in the isotropic case, giving rise to a more complicated NMR spectrum with non-

resolved peaks. To achieve resolution as in the isotropic case, the sample is spun around an axis making an angle of 54.7° with the external magnetic field with a procedure called Magic Angle Spinning (MAS).

A more accurate analysis on the effects of these fluctuations is now presented with the introduction of the Random Fields model.

2.2 Random Fields Model

Considering a set of non-coupled ^{13}C-^{1}H spins system exposed to a large static magnetic field, B_0, usually referred to as oriented along the z-direction of the three-dimensional space, this will be equally experienced by every spin all over the system, leading to a bulk magnetization aligned with B_0. What changes among the nuclear sites is the transverse field, $B_x(t)$, resulting from the previously mentioned mechanisms and randomly fluctuating in time switching between positive and negative values [18]. As a result of the variety of processes occurring in the system, by averaging B_x in the overall set it turns out that:

$$\begin{aligned} \langle B_x(t) \rangle &= 0 \\ \langle B_x^2 \rangle &\neq 0. \end{aligned} \tag{2.2}$$

To obtain a better description of these fields, their average speed of fluctuation can be defined through the autocorrelation function of the total transverse field, $G(\tau)$: this function changes over time assuming non-null values dependent on the time interval τ, with a relation of the form:

$$G(\tau) = \langle B_x(t) B_x(t+\tau) \rangle. \tag{2.3}$$

The correlation function as defined decays with τ: if the time interval between two values of B_x is long compared to the time scale of the fluctiations, then the high probability of having consistence, in terms of sign, between $B_x(t)$ and $B_x(t+\tau)$ is no longer ensured, and an average of their product over the system will tend to zero. This decay of $G(\tau)$ can by now be described by a single exponential equation of the form:

$$G(\tau) = \langle B_x^2 \rangle e^{-\tau/\tau_c}, \tag{2.4}$$

where τ_c is the correlation time of the fluctuations, that means a measure of the rate of motion of the overall random field. Since the exponential part is indipendent on the

size of the averaged fluctuating field, it's useful to define a reduced correlation function, from now on referred to simply as correlation function, $g(\tau)$, hence equal to

$$g(\tau) = \frac{G(\tau)}{\langle B_x^2 \rangle} = e^{-\tau/\tau_c}. \tag{2.5}$$

2.3 Autocorrelation function and spectral density for surfactants in lamellar phase

Referring back to our lamellar phase, the motions influencing the fluctuating fields are, as stated, different in nature and associated with a spread range of time scales: from the fast motions internal to the chain, to slower dynamics occurring throughout the assembly structure. Hence, telling apart these two different regimes of fast (ps - ns) and slow (μs - s) motions, the expression of the correlation function can be improved. Focusing on the fluctuations due to fast motions of the system, these still refer to different processes inside the chain and along the lamellar phase itself: the motions occuring either in the head or in the tail part of the surfactant are different and change their dynamics also going from the very extremities to the central portion of it. As a consequence, the correlation function is better described by a multiexponential decay [15] resulting from the sum of single exponentials each one characterised by a specific correlation time. By weightening the single decays with the distribution of their probabilities, $\mathrm{P}(\tau_c)$, the resulting form is:

$$g(\tau) = \int_0^\infty P(\tau_c) e^{-\tau/\tau_c} d\tau_c. \tag{2.6}$$

Furthemore, the anisotropy of the system and inter and intrachain steric interactions influence the motions, making them, in a way, restricted. In the time window of the current interest, the evolution of $g(\tau)$ would not decay to zero, i.e. the spatial restriction of the motions would not let the system experience every possible orientation. The restriction, represented by the square of the previusly defined order parameter, $\mathrm{S}^2_{\mathrm{CH}}$, will then influence the form of the correlation function representing its plateau value in this time window, obtaining

$$g(\tau) = (1 - S^2_{\mathrm{CH}}) \int_0^\infty P(\tau_c) e^{-\tau/\tau_c} d\tau_c + S^2_{\mathrm{CH}}. \tag{2.7}$$

Regarding now the influence of the motions at a slower time scale (μs to s), these are approximately described with an overall correlation time, τ_s, and a single exponential

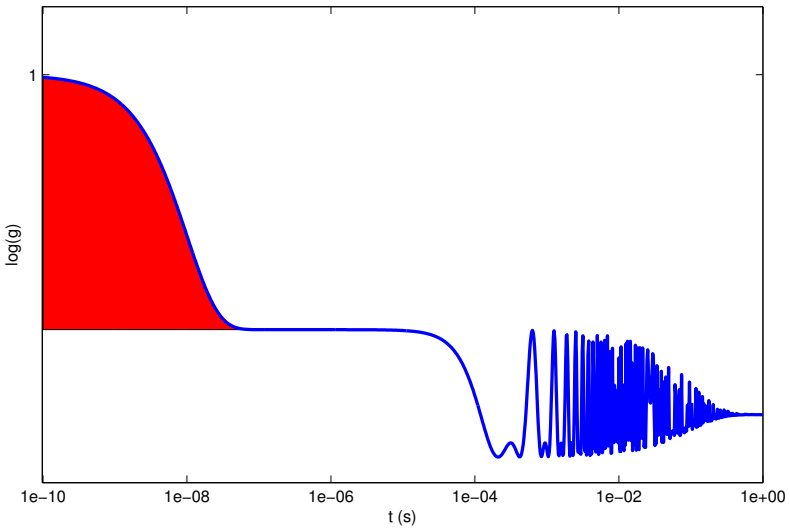

Figure 2.1: Calculated correlation function of a surfactant in lamellar phase of the form expressed in eq. 2.8. The parameters used are: τ_c=10^{-8} s, τ_s=10^{-1} s, S_{CH}=0.5, ω_R=10^4 Hz.

decay function. At last, the effects of spinning the sample at the magic angle with a certain frequency ω_R introduce a modulation of g(τ) represented by the last sum of cosine terms [21] in its eventual expression:

$$g(\tau) = [(1 - S_{CH}^2) \int_0^\infty P(\tau_c) e^{-\tau/\tau_c} d\tau_c + S_{CH}^2] e^{-\tau/\tau_s} [\frac{2}{3} \cos(\omega_R \tau) + \frac{1}{3} \cos(2\omega_R \tau)]. \quad (2.8)$$

Differently from what seen regarding macromolecular systems, this model in regards to surfactants in lamellar phase assumes the correlation function as being affected by two main different motional regimes. These can be clearly told apart by observing the characteristic dependence of $g(\tau)$ on time shown in Fig. 2.1: the correlation function decays at two distinct time regimes, undergoing, inbetween, a plateau value equal to the square of the order parameter S_{CH}^2, as evinceable from eq. 2.8. The reason for the highlighted area will be clarified later on.

The analysis moves on now deriving the Fourier transform of the so-defined correlation function, getting as result the (reduced) spectral density, j(ω). This frequency-domain function still contains the dependence on fast and slow internal motions included in $g(\tau)$, and it will be shown to be also directly related with relaxation rates experimentally evaluated through NMR studies, at specific frequencies.

Defined to be the Fourier tranform of the correlation function, j(ω) can be obtained as

$$j(\omega) = \int_{-\infty}^{\infty} g(\tau) e^{i\omega\tau} d\tau. \tag{2.9}$$

We can now express, through Euler's equality, $e^{i\omega\tau} = \cos(\omega\tau) + i \cdot \sin(\omega\tau)$; the contribution on the integral of the imaginary part is null because of the simmetry of the sin function, hence obtaining

$$j(\omega) = \int_{-\infty}^{\infty} g(\tau) \cos(\omega\tau) d\tau. \tag{2.10}$$

Expliciting the three terms characterising the correlation function in eq. 2.8, j(ω) appears as

$$j(\omega) = \int_{-\infty}^{\infty} (1-S_{\mathrm{CH}}^2)[\int_0^{\infty} P(\tau_c) e^{-\tau/\tau_c} d\tau_c + S_{\mathrm{CH}}^2] e^{-\tau/\tau_s} [\frac{2}{3}\cos(\omega_R\tau) + \frac{1}{3}\cos(2\omega_R\tau)] \cos(\omega\tau) d\tau. \tag{2.11}$$

By distributing now the sum inside the fast-motion part of the correlation function, and by expressing for simplicity the last two terms referring to the slow-motion portion of it as h(τ), we obtain the following expression:

$$j(\omega) = \int_{-\infty}^{\infty} (1 - S_{\mathrm{CH}}^2) \int_0^{\infty} P(\tau_c) e^{-\tau/\tau_c} d\tau_c h(\tau) \cos(\omega\tau) d\tau + S_{\mathrm{CH}}^2 \int_0^{\infty} h(\tau) \cos(\omega\tau) d\tau. \tag{2.12}$$

The contribution related with the fast-motion part of the correlation function will from now on be referred to as g_{MD} because this represents the time portion of this property that can be studied through Molecular Dynamics simulations, as it will be better pointed out later on. Considering now $g'_{MD} = g_{MD} - S_{\mathrm{CH}}^2$, the previous expression can be written in a more compact form as

$$j(\omega) = \mathcal{F}\{g'_{MD} \cdot h(\tau)\} + S_{\mathrm{CH}}^2 \mathcal{H}(\omega). \tag{2.13}$$

The derivation of this integral is now shown by steps.

The solution of the first part of the integral can be illustrated making use of the convolution theorem [22], through which

$$\mathcal{F}\{g'_{MD} \cdot h(\tau)\} = \mathcal{G}'_{MD} \otimes \mathcal{H}(\omega) = \int_{-\infty}^{\infty} \mathcal{G}'_{MD}(\omega') \mathcal{H}(\omega - \omega') d\omega'. \tag{2.14}$$

The Fourier transforms of g'_{MD} and h(τ) are calculated to be as follows:

$$\mathcal{G}_{\mathrm{MD}}(\omega) = 2 \cdot (1 - S^2_{\mathrm{CH}}) \int_0^\infty P(\tau_c) \frac{\tau_c^{-1}}{\tau_c^{-2} + \omega^2} d\tau_c, \tag{2.15}$$

$$\begin{aligned} \mathcal{H}(\omega) = \frac{2}{3}[\frac{\tau_s^{-1}}{\tau_s^{-2} + (\omega + \omega_R)^2} + \frac{\tau_s^{-1}}{\tau_s^{-2} + (\omega - \omega_R)^2}] + \\ + \frac{1}{3}[\frac{\tau_s^{-1}}{\tau_s^{-2} + (\omega + 2\omega_R)^2} + \frac{\tau_s^{-1}}{\tau_s^{-2} + (\omega - 2\omega_R)^2}]. \end{aligned} \tag{2.16}$$

2.3.1 Effective Correlation Time

As it has been stated, the fast motions involved in the dynamics of the system are most probably associated with correlation times $\tau_c < 10^{-6}$ s. On the other hand, the time-scale of the slow motions is mostly on the order of milliseconds. Making use of these conditions, the Fourier transform $\mathcal{F}\{g'_{MD} \cdot h(\tau)\}(\omega_1)$ for frequencies ω_1 in the range of 10^4-10^6 Hz, is found to be equal to

$$\begin{aligned} \mathcal{F}\{g'_{\mathrm{MD}} \cdot h(\tau)\}(\omega_1) = (1 - S^2_{\mathrm{CH}}) \int_0^\infty P(\tau_c) \frac{\tau_c^{-1}}{\tau_c^{-2} + \omega_1^2} d\tau_c = \\ = (1 - S^2_{\mathrm{CH}}) \langle \frac{\tau_c^{-1}}{\tau_c^{-2} + \omega_1^2} \rangle. \end{aligned} \tag{2.17}$$

The function $\mathcal{H}(\omega)$ appears narrow and centered at ω_1, and it is also normalized such that

$$\int_{-\infty}^{\infty} \mathcal{H}(\omega) d\omega = 1. \tag{2.18}$$

Hence, the integral in eq. 2.14 becomes equal to the maximum value of $\mathcal{G}'_{\mathrm{MD}}(\omega)$ multiplied with 1, and the spectral density can be rewritten in the form

$$j(\omega_1) = \mathcal{F}\{g(\tau)\}(\omega) = 2 \cdot (1 - S^2_{\mathrm{CH}}) \langle \frac{\tau_c^{-1}}{\tau_c^{-2} + \omega_1^2} \rangle + S^2_{\mathrm{CH}} \mathcal{H}(\omega_1). \tag{2.19}$$

As it can be seen from eq. 2.23, the spectral density in its eventual expression, apart from the MAS experimental settings, depends on the vaules of the correlation times, τ_cs and τ_s, and the nutation frequency, ω_1. Fig. 2.2 points out the effects of different time-scales motions on j(ω) and on its components, (1-S^2_{CH})$\mathcal{G}'_{MD}(\omega)$ and $S^2_{\mathrm{CH}}\mathcal{H}(\omega_1)$, separately.

The trend of the overall spectral density shows the already presented plateau in a frequency window of ω from 10^4 to 10^7 Hz between the low and high frequency ranges

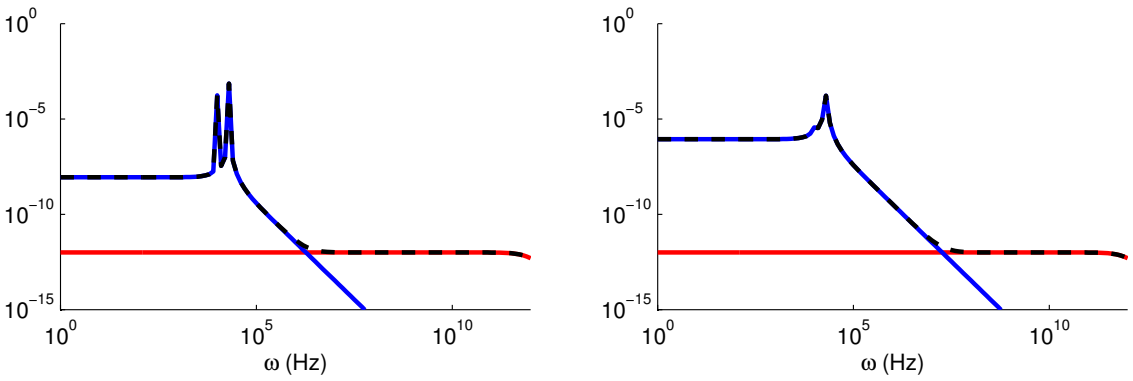

(a) Left: τ_c=10^{-12} s, τ_s=0.1 s. Right: τ_c=10^{-12} s, τ_s=0.01 s.

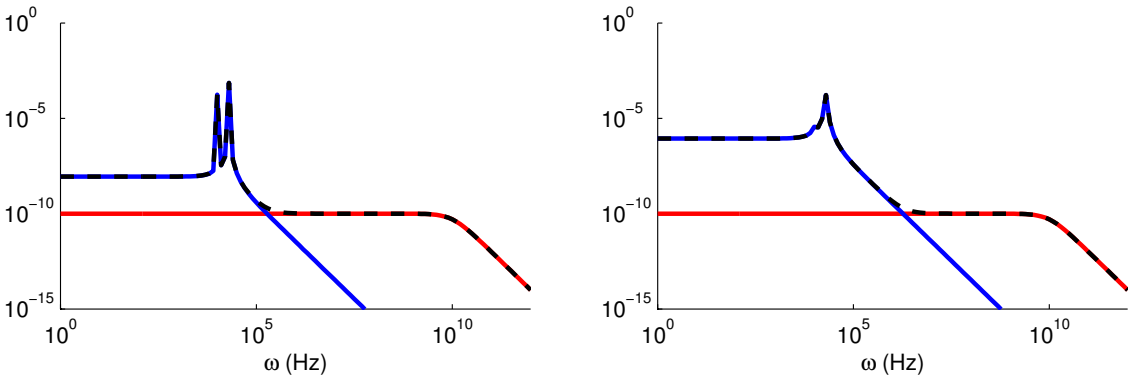

(b) Left: τ_c=10^{-10} s, τ_s=0.1 s. Right: τ_c=10^{-10} s, τ_s=0.01 s.

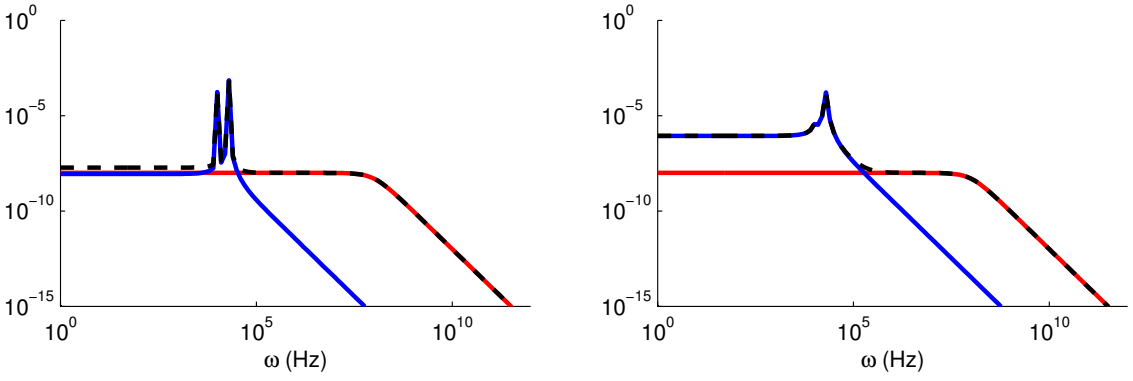

(c) Left: τ_c=10^{-8} s, τ_s=0.1 s. Right: τ_c=10^{-8} s, τ_s=0.01 s.

Figure 2.2: Simulated spectral densities, j(ω) (black dashed line) (eq. 2.13) for different correlation times τ_c and τ_s. The solid line show (1-S^2_{CH})$\mathcal{G}'_{MD}(\omega)$ (red) (eq. 2.15) and $S^2_{CH}\mathcal{H}(\omega_1)$ (blue) (eq. 2.16).

before decaying towards zero (Fig. 2.1). By telling apart the two different contributions on j(ω) (2.13), it can then be seen that, in the plateau window, the slow-motion component of the spectral density has decreased towards zero, leading to a total j(ω) dependent on its fast-motion term, (1-S^2_{CH})$\mathcal{G}'_{MD}(\omega)$, only. Furthemore, by comparing the different orders of magnitude of τ_c and the ω in this range, and hence assuming τ_c^{-2} as being much bigger than ω_1, the denominator of the averaged term in eq. 2.17 can be approximised to τ_c^{-2}, hence leading to the eventual semplification of j(ω) in the plateau range as:

$$j(\omega)_{\text{plateau}} = \mathcal{F}\{g(t)\}(\omega_{\text{plateau}}) = 2 \cdot (1 - S^2_{\text{CH}})\langle\tau_c\rangle. \tag{2.20}$$

The value in brackets in eq. 2.20 represents the effective correlation time, τ_e:

$$\tau_e = \frac{j(\omega_{\text{plateau}})}{2 \cdot (1 - S^2_{\text{CH}})}. \tag{2.21}$$

This quantity defines the time-scale of the fast motions characteristic of the C-H bond, and is the direct measure of the area delimited below g(τ) and the plateau S^2_{CH} divided by (1-S^2_{CH}) shown in red in Fig. 2.1. It corresponds to the overall time-scale of motions characterised by high frequency in a lamellar phase that has been shown to be dynamically influenced by definite and separate motional regimes.

2.3.2 Derivation of τ_e through ^{13}C NMR and MD studies

Through specific pulse sequences exposed later on, ^{13}C NMR experiments can lead to the evaluation, among all, of two observables associated with relaxation mechanisms of the ^{13}C nuclear spins [19, 20]: R_1, rate constant characteristic for longitudinal relaxation, and $R_{1\rho}$, associated with spin-lattice relaxation in the rotating frame; in addition, the NMR technique allows also a direct measurement of the order parameter characteristic of the different C-H bonds, S_{CH} . The two mentioned rate constants are dependent on the spectral density at characteristic frequencies with relations of the form [18, 23, 24]:

$$\begin{aligned} R_1 &= \gamma^2 b^2 j(\omega_0), \\ R_{1\rho} &= \gamma^2 b^2 \frac{1}{2}[j(\omega_1) + j(\omega_0)], \end{aligned} \tag{2.22}$$

with ω_0 and ω_1 being the Larmor and the nutation frequencies respectively, γ being the gyromagnetic ratio of the ^{13}C nucleus and b the root-mean square amplitude of the fluctuating local field. The specific values of ω_0 and ω_1 depend on experimental setting

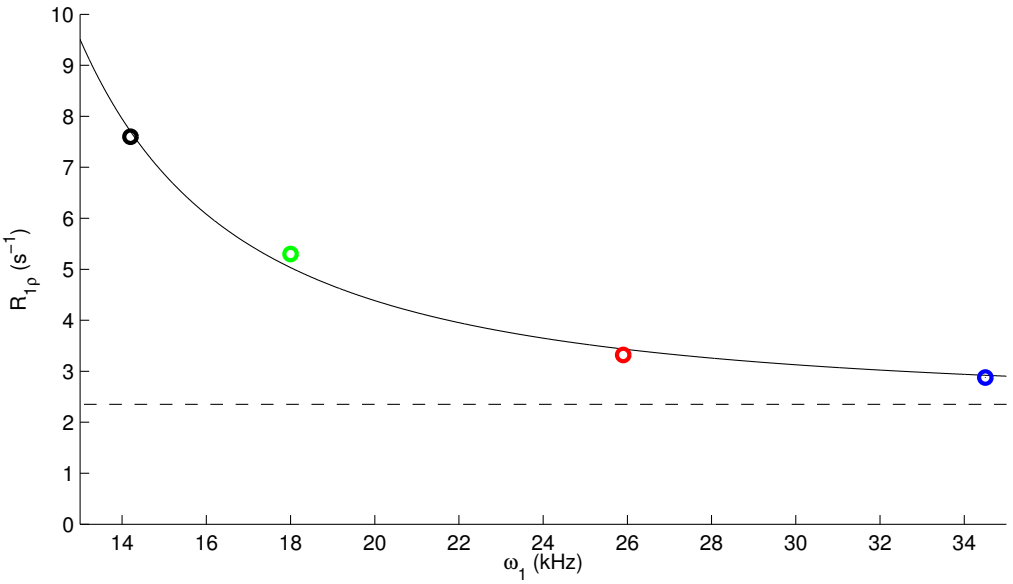

Figure 2.3: $R_{1\rho}$ dependence on nutation frequency ω_1 for ^{13}C nucleus labelled 3 in Fig. 3.2 for $C_{12}E_5/D_2O$ sample with 77 wt% $C_{12}E_5$ at 300° K. The four points correspond to signals acquired at ω_1 14.2 KHz (black), 18 KHz (green), 25.9 KHz (red) and 34.5 KHz (blue).

conditions, and in particular to the intensity of the external magnetic field, B_0, of the order of hundreds of MHz, and on B_1, the field intensity of RadioFrequency pulses implemented in the sequence. The experimental settings of this method allow B_1 to be varied and hence to span the value of ω_1 over a window of frequencies generally from 10^4 to 10^6 Hz.

By acquiring the appropriate pulse sequence over different values of B_1, a set of $R_{1\rho}$ values can be obtained: this rate constant shows to decay with ω_1 in the mentioned time window towards a plateau, as shown in Fig. 2.22

On regards to the form of $R_{1\rho}$ expressed in eq. 2.22, the trend showed by this rate constant reflects the dependence of $j(\omega)$ on the frequency. In particular, the frequency range characterising the plateau reached from $R_{1\rho}$ would correspond to the intermediate region between long and short time scales seen in Fig. 2.2 corresponding to the flat trend of the spectral density.

This evaluation of a frequency characterising $j(\omega)$ in the plateau range let now the method go on to the evaluation of the effective correlation time. In particular, by measuring R_1 and $R_{1\rho}$ at the same B_0 intensity and at an ω_1 within the so-optimised range, from eq. 2.22 the resulting spectral density at the nutation frequency is derived, as

$$j(\omega_1) = \frac{2R_{1\rho} - R_1}{\gamma^2 b^2}. \tag{2.23}$$

This correspondes to measure the spectral density in the plateau region, where, as stated, its frequency-dependence reflects the fast-motion contribution only. Hence, by measuring, as said, the order parameter S_{CH} through fairly accessible NMR analysis, we are able to derive, from eq. 2.20, the value of the effective correlation time τ_e characteristic of the C-H bond through

$$\tau_e = \frac{R_{1\rho} - \frac{1}{2}R_1}{\gamma^2 b^2} \cdot \frac{1}{1 - S^2_{CH}}. \tag{2.24}$$

To make the point of what presented until now and sketch the aim of the next section, it can be summarised that common ^{13}C NMR analysis allow to draw a picture of the dynamics of the systems in terms of an averaged τ_s and hence to optimise the experimental settings by choosing a proper order of magnitude for the nutation frequency, ω_1. By achieving this, again, through fairly easy ^{13}C NMR studies, as it will be better shown in the next section, one is able to derive, aside from the order parameter, S_{CH}, two rate constants, R_1 and $R_{1\rho}$, that map the spectral density at different frequencies. The combination of those leads to the derivation of $j(\omega_1)$ and hence of the effective correlation times τ_e characterising the dynamics throughout the chain.

Together with the ^{13}C NMR study, another approach is represented by Molecular Dynamics simulations of the system [25, 26], from which, as it will be described, to obtain the different autocorrelation functions characteristic of the sites of the molecule. Even though the time-scale of an MD symulation doesn't allow to reproduce processes occurring in the slow-motion time regime, for what stated regarding this context, the correlation function in eq. 2.8 can be truncated at its first term without loosing the the reliability of the derived spectral density with regards to the inter- and intra-molecular motions. Hence, the derivation of $g(\tau)$ over the simulations allows to calculate the effective correlation time directly from the area described by the function until the reach of the plateau (Fig. 2.1). Furthemore, by Fourier transforming the optimized form of the correlation functions and by calculating the order parameter directly from the MD results, the value of $j(\omega)$ at the Larmor and nutation frequency is derived, through which to calculate R_1 and $R_{1\rho}$ relaxation rates (eq. 2.22) compareable with the NMR experimental measurements.

2.4 Amphiphilic Systems

Lipids and surfactants are amphiphilic molecules possessing both a hydrophilic head group and a hydrophobic alkyl tail [1]. In water, such systems aggregate in self-assemblied structures that lead to an adequately hydration of the polar head part, while preventing the alkyl chain from exposure toward the aqueous environment. Aside from the chemical nature of the surfactant, that determines the morphology of the arrangement, the characteristics of the specific self-organised structure are influenced also by external conditions as concentration, temperature, pressure and nature of the solvent. The resulting transition between phases has different dependeces towards several variables and this makes it controllable through changes of intensive properties.

In regards to what will be the subject of this study, the nonionic surfactant in analysis is pentaethyleneglycol mono n-dodecyl ether, abbreviated as $C_{12}E_5$ [27]: this molecule is composed by an hydrophobic saturated alkyl chain made of 12 carbon atoms, and a hydrophilic head possessing 5 units of ethilen glycol linearly bound. By according to the phase diagram reported by Imai *et al.* [28], the temperature and concentration parameters had been chosen whithin the range of the lamellar phase region. In particular, the ordered self-assemblied structure characterising this phase corresponds to a lamellar phase, a membrane made of two layers of molecules exposing the hydrophilic heads towards a layer of water. In this structure, the individual surfactant molecules show high mobility and can rapidly exchange and diffuse whithin the plane of the bilayer, while their orientation keeps ensured, giving to the system an overall anisotropic behaviour ascribable to a liquid crystal phase.

Chapter 3

^{13}C NMR Analysis

3.1 Method

Focusing the attention now on the Nuclear Magnetic Resonance, this technique can lead to an insight of, among all, two different mechainisms of relaxation: longitudinal, or spin-lattice, relaxation and spin-lattice relaxation in the rotating frame. Two different ^{13}C NMR experiments are presented that allow to study these two features, starting with the former.

3.1.1 Inversion-Recovery INEPT Pulse Sequence

When a system containing a set of 1/2-spins is perturbated by a strong and static external magnetic filed aligned with a direction, say z, of the reference space, the nuclear magnetic moments of the spins would tend to align with it: the result is then a bulk magnetization along the z-direction, and a null net transverse magnetization in the orthogonal plane. This derives from the absence of a preferential orientation of the x and y components of the nuclear magnetic moments [19]. If then a RadioFrequency pulse, or a sequence of it, is applied in the x,y-plane, the equilibrium magnetization is rotated towards the transverse plane: its consequent longitudinal relaxation about the z-axis at the Larmor frequency will reastabilish the equilibrium orientation. The multiple-pulse sequence aimed to study this process is schematised in Fig. 3.1a. The acquired signal will result from the coherence transfer from ^{1}H to ^{13}C: this is evolved throughout the first part of the sequence, known as INEPT (Insensitive Nuclei Enhanced by Polarization Transfer) [29, 30]. An overview of the processes involved in this analysis is now presented.

An initial 90° RF pulse on resonance with the proton Larmor frequency rotates the

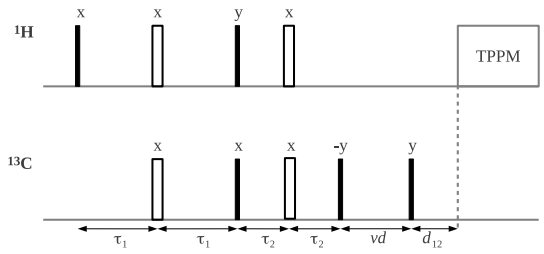

(a) Inversion-Recovery INEPT

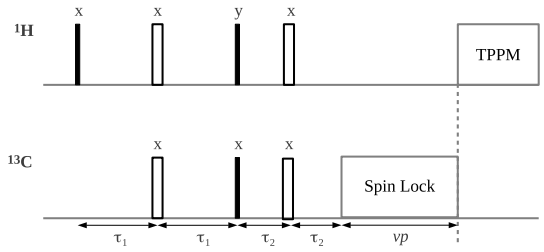

(b) Spin-Locking INEPT

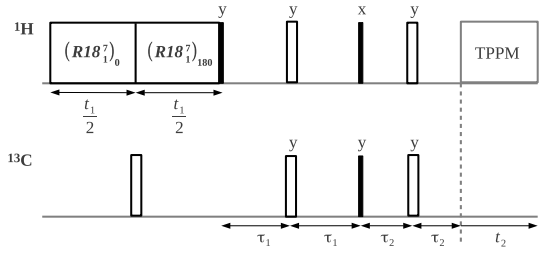

(c) R-PDLF

Figure 3.1: Pulse sequences in the three different ^{13}C NMR experiments.

^{1}H magnetization on the transverse plane (-y direction); during the following spin-echo involving both ^{1}H and ^{13}C spins, the offset, e.g. the angle through which the magnetization has been precessed during the first τ_1, is refocused at the end of the second period of the same time-length through the intermediate 180° pulse. What evolves for the whole of the spin-echo is the magnetization component due to the coupling between ^{1}H and ^{13}C: the following pair of 90° RF pulses would now affect this coupled term, leading to the transfer of the anti-phase state from ^{1}H to ^{13}C. In order to acquire an in-phase signal, another spin-echo sequence follows, differing from the first one only in terms of the chosen time interval τ_2: this will determine an overall transverse magnetization on the ^{13}C spin, though proportional in size to the equilibrium magnetization of ^{1}H initially perturbated and source of the coherence transfer. At last, the acquisition occurs after an inversion-recovery pulse sequence, adapted to the so far obtained evolution of the magnetization. The in-phase transverse magnetization of the ^{13}C spin along the x-direction is rotated towards the z-axis through the first 90° pulse, and afterwards allowed to relax for the time interval *vd*. After this, the last 90° pulse inverts the magnetization towards the x-direction, and the resulting Free Induction Decay is detected. During the acquisition of the ^{13}C signal, a broadband decoupling of the ^{1}H spins is applied through a Two-Pulse Phase Modulation (TPPM): this removes the splitting of the signal due to ^{1}H-^{13}C dipolar couplings and makes multiplet peaks collapse into single line, while enhancing the intensity and hence the sensitivity of the spectrum.

The analysis of the collected data starts with a convertion of the time-dependent signal into a frequency-domain spectrum: the Fourier Transform of the data leads to the observation of absoprtion Lorentzian peaks of the form:

$$S(\omega) = c \cdot \frac{\lambda}{\lambda^2 + (\omega - \omega_0)^2}, \tag{3.1}$$

where ω_0 is the Larmor frequency of the involved resonant ^{13}C nucleus, λ is the coherence decay rate constant and c is the proportionality constant between the height of the acquired signal and the one of the peak obteinable with a time delay vd=0. Since the height of the peak is proportional to the size of the z-magnetization of the spins just before the last 90° pulse, iterating the acquisition over a range of different time delays allows to obtain a set of signals with an height decaying with *vd* through an exponential fashion of the form

$$S(t) = c \cdot e^{-t/T_1}. \tag{3.2}$$

The rate of the decay corresponds to $R_1=\frac{1}{T_1}$, the longitudinal relaxation rate constant, that is equal to $\gamma^2 b^2 j(\omega_0)$.

3.1.2 Spin-Locking INEPT Pulse Sequence

The other mechanism studied is the spin-lattice relaxation in the rotating frame, and the pulse sequence executed for this purpose is shown in Fig. 3.1b. After an initial INEPT sequence leading to the evolution of the magnetization as already described, the resulting in-phase magnetization of ^{13}C ends up aligned with the x-axis. If now a strong RF field, B_1, is applied in the rotating frame, the magnetization finds itself aligned with it, and is said to be spin-locked [23]. As strong as it can be, the filed created during this process would anyway be much smaller than the external one, B_0: the magnetization, while mantained aligned with it, will start decaying in magnitude with time towards a value B_1/B_0 smaller than the initial one. Iterating the acquisition over a range of spin-locking times, the decay of the observed signal height would now be associated with

$$S(t) = c \cdot e^{-t/T_{1\rho}}, \tag{3.3}$$

with $R_{1\rho}=1/T_{1\rho}$ being the rate of the relaxation in the rotating frame, being equal to $\frac{1}{2}\gamma^2 b^2[j(\omega_0) + j(\omega_1)]$.

3.1.3 R-PDLF Pulse Sequence

The last ^{13}C NMR study allows to derive the order parameter, S, characteristic of the different C-H bonds throughout the surfactant chain. This is achieved by applying a two-dimensional recoupling method [31, 32, 33] , schematically shown in Fig. 3.1c.

This pulse sequence represent a Recoupled-type scheme folowed by a Proton Detected Local Field protocol (R-PDLF). It starts with a rotor-synchronizedsequence, $R18_1^7$, that consists of a repetitive scheme of $180^\circ_{70}180^\circ_{-70}$ RF pulse pairs, where each 180° pulse occupies 1/18 of a rotor period. Applied to ^1H spins, this irradiation leads to the recoupling of the ^1H-^{13}C dipolar couplings and ^1H chemical shift anysotropy, while the homonuclear dipolar interaction among protons is suppressed. Afterwards, another $R18_1^7$ sequence is implemented for the same time length: setting the overall phase shift between the two R blocks and by applying at their junction a ^{13}C 180° pulse, the ^1H CSA term is partially suppressed, while the ^1H-^{13}C dipolar coupling is retained. The ^1H polarization evolved during t_1 is then transferred to ^{13}C spins through a rotor-synchronised INEPT sequence

acting as previously described, and leading to the detection of the ^{13}C FID under TPPM proton decoupling during t_2.

In this sequence, two different time lengths can be modulated: the ^{1}H polarization evolves during the $R18_1^7$ irradiations, thus changes in the evolution time period t_1 modulate the effect of the ^{1}H-^{13}C dipolar coupling on that. This polarization is then transferred to ^{13}C spins and detected during t_2. A 2-D FID is hence acquired by assemblying 1-D FID referring to an increasing value of t_1. By performing the Fourier transform in both the dimensions t_1 and t_2, a 2-D spectrum is obtained. The splitting, $\Delta\nu_{CH}$, in terms of frequency, of each ^{1}H-^{13}C spin pair, depictable from the 2-D spectrum, is proportional, in our conditions of fast motions inside the system, to the segmental order parameter S_{CH}, since

$$\begin{aligned} \Delta\nu_{\mathrm{CH}} &= 0.315 \cdot (-\frac{\mu_0}{4\pi}) \cdot \frac{\gamma_H \gamma_C \hbar}{r^3} \cdot (3\cos^2\theta - 1); \\ S_{\mathrm{CH}} &= \frac{1}{2}\langle 3\cos^2\theta - 1\rangle. \end{aligned} \tag{3.4}$$

with γ_H and γ_C being proton and ^{13}C gyromagnetic ratios respectively, r the internuclear distance between the two atoms and θ the angle between the internuclear vector and the magnetic filed axis.

3.1.4 Experimental Details

Pentaethylene glycol dodecyl ether ($C_{12}E_5$) with a purity higher than 99.8% was mixed with deuterium oxide (D_2O) in samples containing 57, 70 and 77 wt% of surfactant by weighing the respective amount of surfactant and water into vials, mixing them in a vortex mixer and centrifuging them in order to remove air bubbles.

The experiments were performed using a Bruker Avance AVII-500 NMR spectrometer operating at ^{1}H frequency of 500.23 MHz equipped with a standard bore CP_{MAS} HX probe. All the experiments were done at a spinning frequency of 5 KHz.

3.1.5 Analysis

The ^{13}C NMR spectrum of a $C_{12}E_5/D_2O$ mixture with 62 wt% $C_{12}E_5$ at 300° K acquired using the Inversion-Recovery INEPT method is shown in Fig. 3.3. The peak assignments are made on the basis of previous works [27], and refer to the labelling shown in Fig. 3.2.

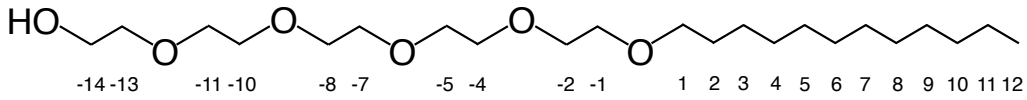

Figure 3.2: Carbon labelled $C_{12}E_5$ molecule.

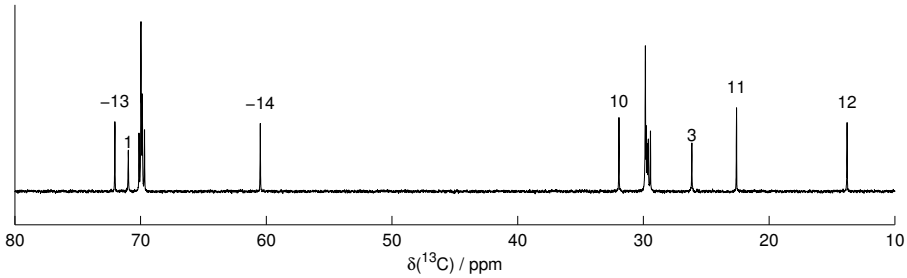

(a)

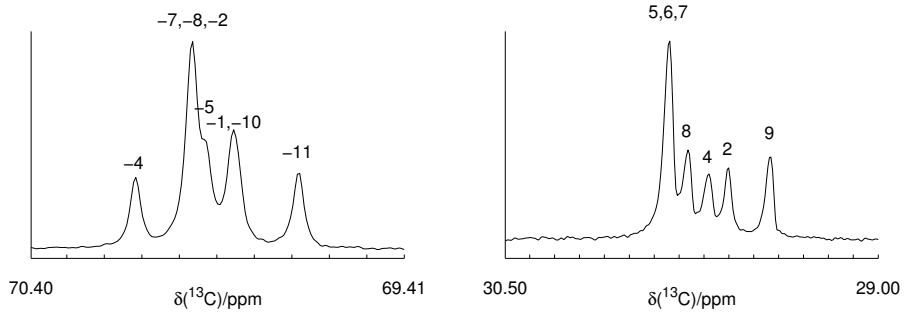

(b)

Figure 3.3: (3.3a) ^{13}C NMR spectrum of a $C_{12}E_5/D_2O$ mixture with 62 wt% $C_{12}E_5$ at 300° K. (3.3b) The assignements for the two multi-peaks in the overlapped regions of the spectrum are separetely shown.

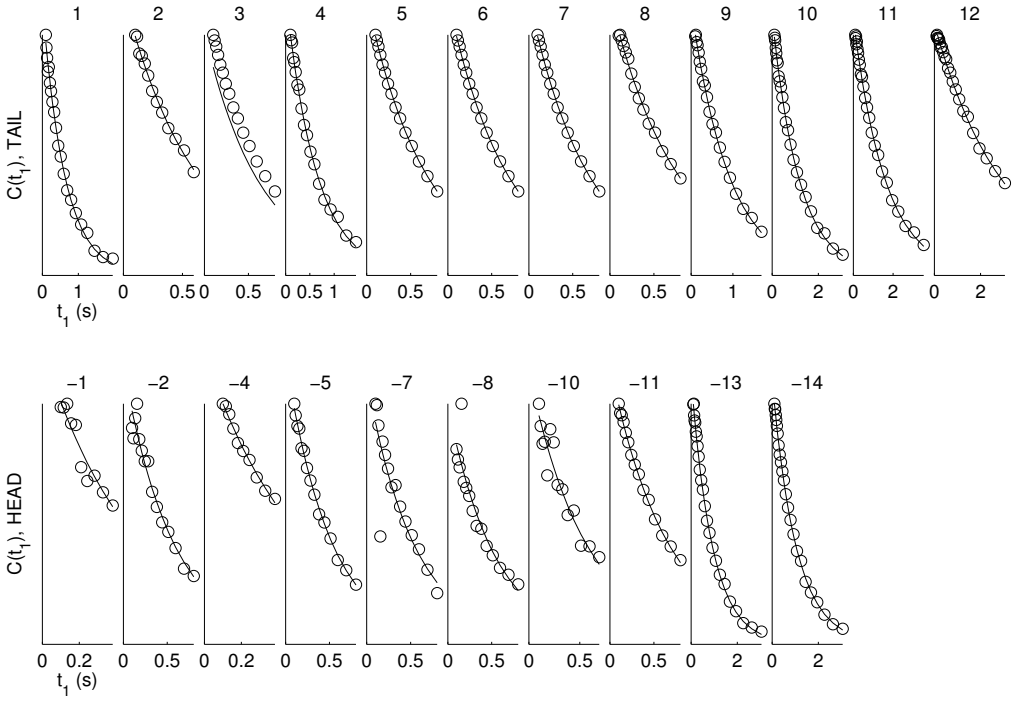

Figure 3.4: Signal height decay (eq. 3.2) for the single ^{13}C nuclei throughout the $C_{12}E_5/D_2O$ with 62 wt% $C_{12}E_5$ at 300° K.

As described, the signal of each ^{13}C nucleus of the molecule obtained with either Inversion-Recovery INEPT or Spin-Locking INEPT is studied throughout the whole aquisition process in order to obtain, eventually, its characteristic values of the relaxation frequencies, R_1 and $R_{1\rho}$.

In detail, each peak resulting from the first acquisition process with a time delay (named *vd* for the Inversion-Recovery INEPT sequence and *vp* for the Spin-Locking sequence, as in Fig. 3.1a - 3.1b) of 0.1 s is fitted with a Lorentzian curve of the form presented in eq. 3.1. This first fitting is aimed to optimise all c, λ and ω parameters. Differently, for all the 31 following acquisitions, the so-obtained λ is considered stable enough to be fixable, optimising then c and ω only.

The derivation of the R_1 and $R_1\rho$ parameter of the different ^{13}C nuclei along the chain is achieved by fitting the decay of c optimised over the whole acquisition process with an exponential function of the form expressed in eq. 3.2. The different trends of the characteristic decays throughout the sites of the molecule are shown in Fig. 3.4.

Due to the chemistry of the molecule, the resonances of some ^{13}C nuclei are so close in

frequency that the corresponding signals are not resolved but end up overlapping into the two broad multipeaks presented in Fig. 3.3b. The procedure to deal with the evaluation of the two relaxation constants of the involved nuclei is the following. The signal of each ^{13}C site expected to give resonance at a particular frequency in the overlapped region is associated with a Lorentzian curve, itself optimised in all its c, λ and ω parameters, as previously described. The overall multipeak is then fitted by the resulting function, still of Lorentzian form, given by the sum of all the expected fitting curves. The procedure through which to obtain each R_1 and $R_{1\rho}$ values reflects the one already presented for the other single peaks of the spectrum. In these two cases of overlapping regions, both the evaluation of the ω trend and of the decay of c throughout the acquisition process are carried on for each single fitting curve involved.

All the fitting analysis are obtained through the uncostrained function "fminunc" of Matlab [34], that uses as default the algorithm "trust-region-reflective". Constrained conditions are though needed in order to fit the multipeak appearing in the 69.4 – 70.4 ppm range: in this case the Matlab function used is "fmincon", choosing the same algorithm as before.

Chapter 4

Molecular Dynamics (MD) Simulations

4.1 Method

The classical Molecular Dynamics simulations are performed with Gromacs 4.5.3 software package [35]. The initial structure is composed of symmetric and planar bilayer constructed from 512 $C_{12}E_5$ molecules and 3168 water molecules, with the corresponding mass fraction of 80 wt% in surfactant. GROMOS 45A3 force field [36, 37] is used to describe the the alkyl tail of the $C_{12}E_5$ molecules; in order to properly describe the nonionic ethylene-oxide head and better reproduce the hydrophilicity of this portion [38], a recently suggested modification of the GROMOS 45A3 force field for EO chains is chosen [39]; Simple Point Charge (SPC) water model is used for water [40]. The pressure is coupled at 1 bar by using isotropic Parrinello-Raman pressure coupling with coupling constant of 1.0 ps and compressibility of $4.5{\cdot}10^{-5}$ $(\text{bar})^{-1}$ [41, 42]; temperature is coupled at 300 K by using Nose-Hoover thermostat with time constant of 0.1 ps [43]. A cut-off scheme is chosen for short-range nonbonded interactions, with a van der Waals radius of 1.4 nm. Electrostatics are computed using Particle Mesh Ewald (PME) summation [44]; the used time step is of 2 fs. Bond lengths in surfactant molecules are constrained using LINCS [45], while water geometry is constrained using SETTLE [46]. The total simulation time takes 406 ns, but only the last 226 ns are used for the further analysis, since the initial 180 ns are considered to be required for the system to equilibrate. The MD trajectories are saved every 10 ps.

Since a united atom force field is used, the hydrogren atoms are not explicitly present

in the simulation. In order to calculate order parameters and rotation correlation functions for the C-H bonds, the hydrogen trajectories are constructed afterwards by assuming a C-H bond length of 0.112 nm and an ideal tetrahedral geometry.

4.2 Analysis

For each C-H bond, the trajectory of the associated unit vector $\vec{\mu}(\tau)$ over the simulation time is converted to the correlation function g_{MD} and the order parameter $\mathrm{S_{CH}}$ through the following ensemble averagings respectively:

$$g(\tau) = \langle P_2[\vec{\mu}(t+\tau) \cdot \vec{\mu}(t)] \rangle_t, \tag{4.1}$$

$$S_{\mathrm{CH}} = \langle P_2[\vec{\mu}(t) \cdot \vec{n}] \rangle_t, \tag{4.2}$$

where $\mathrm{P}_2(x) = (3x^2 - 1)/2$ is the second Legendre polynomial and $\vec{n}$ is the symmetry axis of the bilayer. The effective correlation time τ_e is now directly calculated from the area described by $g(\tau)$ from time zero until the time τ_p of the reach of the plateau value $\mathrm{S^2_{CH}}$:

$$\tau_e = \frac{\int_0^{\tau_p} g(\tau) d\tau}{1 - S^2_{\mathrm{CH}}}. \tag{4.3}$$

In order to derive the relaxation rates R_1 and $\mathrm{R}_{1\rho}$ as a comparison with the NMR results, the evaluation of the spectral density $\mathrm{j}(\omega)$ now follows: the method refers to a recently presented approach for the calculation of the Fourier transform of the correlation function, here summarised. Due to the time scale of near-atomistic MD simulations, performed up to the order of hundreds of ns, $g_{\mathrm{MD}}(\tau)$ is associated with the fast-motion contribution of the total correlation function $g(\tau)$, (eq. 2.7) and hence, as shown, expressed by the continuous distribution of exponential correlation times and as decaying to a non-zero plateau equal to $\mathrm{S^2_{CH}}$, as

$$g_{\mathrm{MD}}(\tau) = g(\tau) = (1 - S^2_{CH}) \int_0^{\infty} P(\tau_c) e^{-\tau/\tau_c} d\tau_c + S^2_{CH}, \tag{4.4}$$

with $\mathrm{P}(\tau_c)$ being the continuous probability distribution of correlation times τ_c. Considering now the reduced and normalized correlation function g'_{MD} of the form

$$g'_{\mathrm{MD}}(\tau) = \frac{g_{\mathrm{MD}}(\tau) - S^2_{CH}}{1 - S^2_{CH}} = \\ = \int_0^\infty P(\tau_c) e^{-\tau/\tau_c} d\tau_c, \tag{4.5}$$

the continuous distribution $\mathrm{P}(\tau_c)$ is approximated as a large number of discrete components j with correlation time $\tau_{c,j}$ and weight p_j:

$$P(\tau_c) = \sum_{j=1}^{M} p_j \delta(\tau_c - \tau_{c.j}). \tag{4.6}$$

The set of p_j is estimated by minimizing the following relation

$$V = \sum_{i=1}^{N} \sum_{j=1}^{M} (g'_i - p_j e^{-\tau_i/\tau_{c,j}})^2, \tag{4.7}$$

with $g'_i = g'_{\mathrm{MD}}$ for a discrete set of times τ_i, the values of p_j constrained to be non-negative, and eq. 4.7 in practice fitted with a least-square algorithm.

With p_j and τ_j coming from the described fitting procedure (eq. 4.7) of each correlation function obtained through eq. 4.1 and S_{CH} also calculated directly from the simulations by using eq. 4.2, the resulting correlation function referring to the time window covered by the MD analysis appears now as

$$g_{\mathrm{MD}}(\tau) = (1 - S^2_{\mathrm{CH}}) \sum_{j=1}^{M} p_j e^{-\tau/\tau_c} + S^2_{\mathrm{CH}}, \tag{4.8}$$

leading, for what presented in eq. 2.8, to an overall form for $\mathrm{g}(\tau)$ as

$$g(\tau) = g_{\mathrm{MD}}(\tau) e^{-\tau/\tau_s} [\frac{2}{3} \cos(\omega_R \tau) + \frac{1}{3} \cos(2\omega_R \tau)]. \tag{4.9}$$

The corresponding spectral density is then derived by calculating the Fourier transform of eq. 4.9 as

$$j(\omega) = (1 - S^2_{\mathrm{CH}}) \sum_{j=1}^{M} p_j K(\omega, \tau_{c,j}) + S^2_{\mathrm{CH}}, \tag{4.10}$$

where

$$
\begin{aligned}
K(\omega,\tau_c) = \quad & \frac{1}{3}\sum_{j=1}^{M} \frac{\tau_c^{-1}+\tau_s^{-1}}{(\omega+\omega_R)^2+\tau_c^{-2}+\tau_s^{-2}} \quad + \\
& + \quad \frac{\tau_c^{-1}+\tau_s^{-1}}{(\omega-\omega_R)^2+\tau_c^{-2}+\tau_s^{-2}} \quad + \\
& + \quad \frac{1}{6}\sum \frac{\tau_c^{-1}+\tau_s^{-1}}{(\omega+2\omega_R)^2+\tau_c^{-2}+\tau_s^{-2}} \quad + \\
& + \quad \frac{\tau_c^{-1}+\tau_s^{-1}}{(\omega-2\omega_R)^2+\tau_c^{-2}+\tau_s^{-2}} \quad ,
\end{aligned}
\tag{4.11}
$$

with ω_R being constant. and equal to the Magic Angle Spinning frequency.

Through this eventual form of the spectral density, the effective correlation time τ_e can be now evaluated and used to test the derivation achieved through the experimental ^{13}C NMR studies. In particular, by calculating the so-defined j(ω) at a frequency ω_1 in the range of the plateau value (1-S^2_{CH}) of the spectral density, the effective correlation time is the derivable, as shown by eq. 2.21.

Furthemore, the calculation of the spectral density at ω_0, ω_1 and ω_R, corresponding respectively to Larmor, nutation and MAS frequencies characterising the ^{13}C NMR experiments, allows a comparison between the experimental results concerning the rate constants R_1 and $R_{1\rho}$ as from eq. 2.22.

4.3 Analysis Details

Each correlation function obtained from the simulations through eq. 4.1 is fitted with a function of the form of eq. 4.8 by minimizing the probability distribution as in eq. 4.7 for a set M=71 δ-functions with exponential spacing of $\tau_{c,j}$ between 100 fs and 1 μs. The optimization is achieved by using the "lsqnonneg" function in Matlab [34].

Chapter 5

Results and Discussion

5.1 R_1 and $R_{1\rho}$ Rate Constants

The experiments referring to the Inversion-Recovery pulse sequence had been acquired for samples at different concentrations of surfactant and at different temperatures, and the resulting R_1 values are presented in Fig. 5.1.

The general trend of the different values of R_1 throughout the ^{13}C sites of the chain confirms what expected concerning the various mobilities [47]. Because of the higher freedom of motions of the ending sides of the molecule, the nuclear magnetic moments of these external ^{13}C nuclei would take a longer time to relax and get back to their equilibrium orientation. The lowest R_1 rates are then observed for the very last portions of the chain, and increase towards its central part. Regarding the dependence of this parameter on the temperature, the general effect of highering T is to raise the rate of motions inside the system, resulting in the observed decrease of R_1. Aside from this common behaviour, a greater sensitivity is observed for the nuclear sites of the ethylene oxide portion of the chain, interpreted in light of a known temperature-dependence of this class of molecules [48, 49]. In particular, in stable conditions the conformation of the C–C bonds of the oxide fraction is predominantly *gauche*: this leads to a higher dipole moment and hence to a more favorable interaction with the water molecules in the surroundings. By raising the temperature, the fraction of *trans* conformers tends to increase, resulting in a reduction of the dipole moment and a less favorable interaction with the solvent. The mobility of the head part of the surfactant results then raised because of this additional contribution, determining the more visible lowering of the corresponding R_1 values observable in the Fig. 5.1 - Left. Since the alkyl chain is not concerned with such a interaction, but

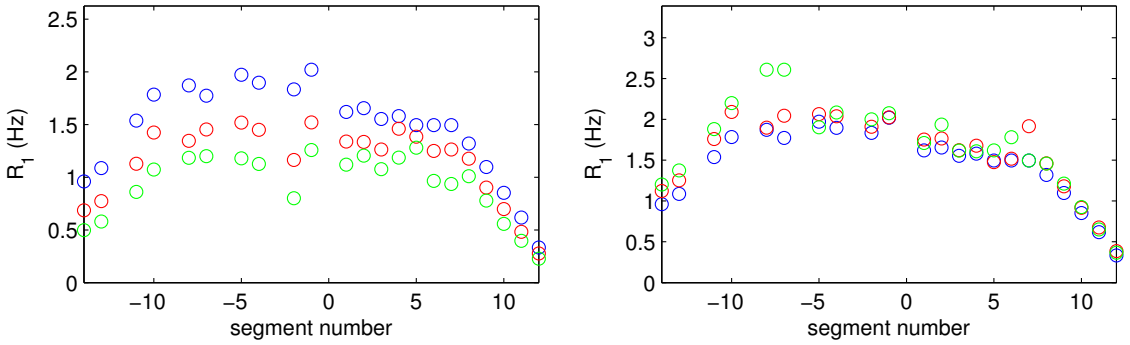

Figure 5.1: Longitudinal relaxation rate constant R_1 for the different ^{13}C sites in $C_{12}E_5/D_2O$. Left: values for samples of 62 wt% of surfactant at 300° K (blue), 310° K (red) and 320° K (green). Right: values for samples of 62 wt% (blue), 70 wt% (red) and 77 wt% (green) of surfactant at 300° K.

rather moving in an hydrophobic environment, its nuclear sites appear to be less sentitive to changes of the temperature. The right side of Fig. 5.1 shows the dependece of the longitudinal relaxation on the surfactant weight percent. Since for all the three analysed samples the surfactant concentration is still whithin the range of the lamellar phase region, the observed slight changes, if any at all, in the R_1 values were expected.

5.2 Optimization of ω_1 and evaluation of τ_e

Different Spin-Locking INEPT experiments are run by changing the magnetic field of the RF pulses, B_1, and hence the nutation frequency, ω_1. The results are shown in Fig. 5.3b. In particular, four different series of acquisition are executed for pulse sequences at the nutation frequencies ω_1 34.5 KHz, 25.9 KHz, 18 KHz and 14.2 KHz. Each signal decay is analysed as described (eq. 3.1) and the exponential decay of the average trend for each set of acquisitions is fitted (eq. 3.3), as shown in Fig.5.3a. The resulting frequency-dependence of $R_{1\rho}$ is evaluated and shown in Fig. 5.3b: the rate constant appears to decay with the increasing of the nutation frequency towards a non-zero value estimated from the fitting procedure. The study of this trend allows to evaluate the proper ω_1 from which to derive the spectral density value as from eq. 2.23.

To the regards of our experimental settings, the NMR acquisitions refer to a ω_1 (25.9 Hz) lower than the optimized value characterizing the plateau trend of $R_{1\rho}$ (35 Hz) (Fig. 5.3b): an evaluation of the error on the spectral density corresponding to the experimental

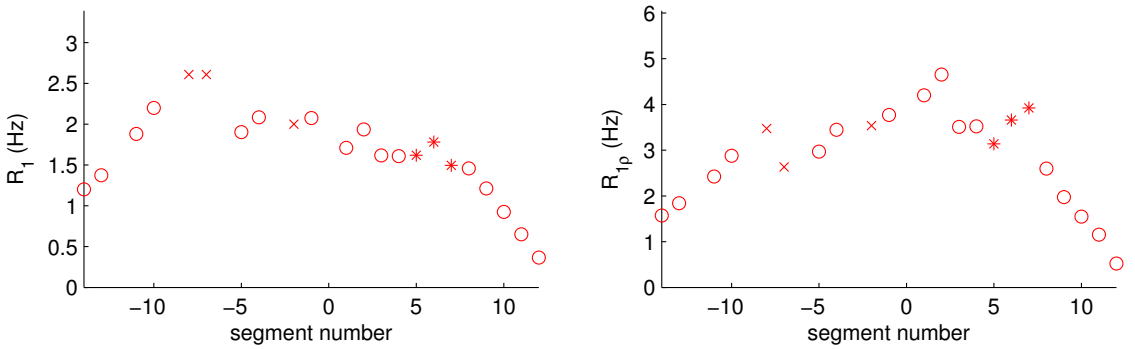

Figure 5.2: Longitudinal relaxation, R_1, and spin-lattice relaxation in the rotating frame, $R_{1\rho}$, for the different ^{13}C sites in $C_{12}E_5/D_2O$ (lamellar phase with 77 wt% of surfactant) at 300° K. Crosses and stars refer to carbons labelled -2; -7; -8 and 5; 6; 7, giving rise to the two triplet peaks shown in Fig. 3.3b.

ω_1 outside the frequency range of interest is then achieved. By combining eq. 2.22 with eq. 2.23 it can be seen that evaluating the rate constant at a ω_1 below the plateau frequency window (Fig. 2.2) leads to an error on $R_{1\rho}$ corresponding to

$$\Delta\mathcal{H}(\omega) = \frac{2\Delta R_{1\rho}}{b^2\gamma^2 S_{\mathrm{CH}}^2}. \tag{5.1}$$

The error contribution on the measured $R_{1\rho}$ is shown in Fig. 5.4 - Left . The evaluated values of the corrected effective correlation times τ_e are achieved referring to eq. 2.23, and shown in Fig. 5.4 - Right. The order of magnitude characterizing the different τ_e confirms what stated concerning the time-scale of the fast motions in the lamellar phase dynamics. Furthemore, the trend of the different values throughout the sites of the molecule reflects the inner distinction of the molecular fragments regarding their mobility.

5.3 MD results and MD-NMR comparison

Snapshots taken from the molecular dynamics simulation of the surfactant are shown in Fig. 5.5. The simulated system shows the self-assembly of the surfactant molecules in lamellar phase; the formation of pores within the phase is also observed, and better evinceable from Fig. 5.5b. The comparison between the S_{CH} order parameters obtained from the MD simulation results (eq. 4.2) and the NMR experimental values are shown in Fig. 5.6: the great accordance between the results achieved with the two different methods is considered as an indication of the accurate description of the system in the simulated

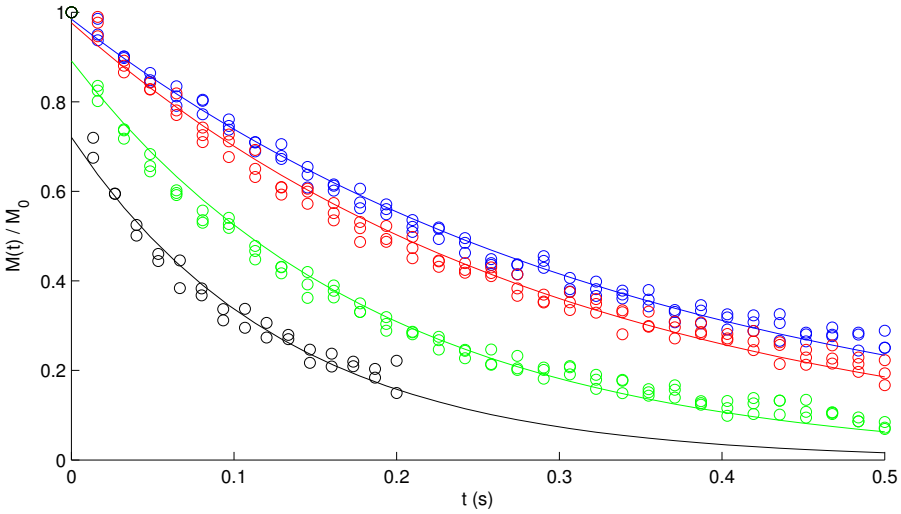

(a)

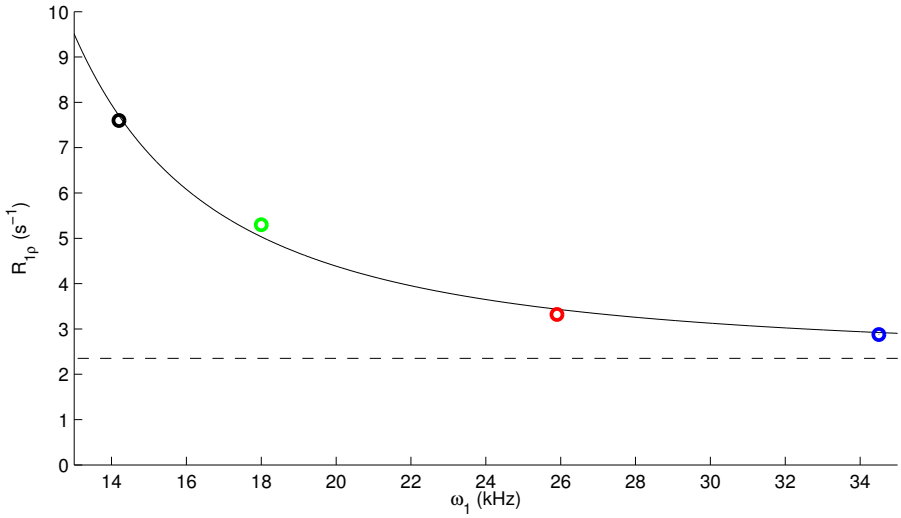

(b)

Figure 5.3: $R_{1\rho}$ dependence on nutation frequency ω_1 for ^{13}C nucleus labelled 3 in Fig. 3.2 for $C_{12}E_5/D_2O$ sample with 77 wt% $C_{12}E_5$ at 300° K.(Fig. 5.3b). Fig. 5.3a shows the single height decays (eq. 3.2) for the for the signals acquired with ω_1 14.2 KHz (black), 18 KHz (green), 25.9 KHz (red) and 34.5 KHz (blue).

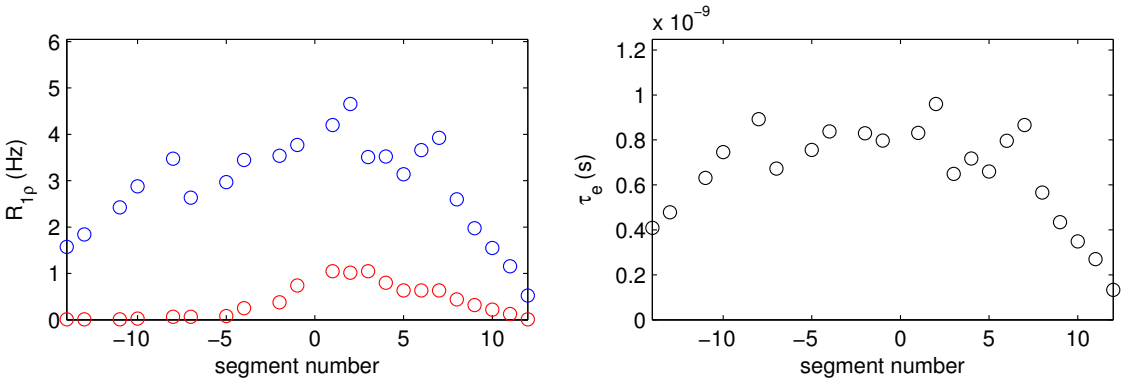

Figure 5.4: Left: (blue) Spin-lattice relaxation in the rotating frame, $R_{1\rho}$, for the different ^{13}C sites in $C_{12}E_5/D_2O$ (lamellar phase with 77 wt% of surfactant) at 300° K acquired at ω_1=25.9 KHz and associated error $\Delta\mathcal{H}(\omega)$ (eq. 5.1)(red). Right: corresponding effective correlation time τ_e obtained through eq. 2.24.

model. Not only, but the shown agreement with the experimental measurements makes the presence and the influence of the observed pores acceptable and well-described by the defined system.

Though, this unexpected discontinuity of the lamellar phase somehow compromises the further analysis on the results of the MD simulations: as can be better seen from Fig. 5.5b, due to the artifact of the periodic boundary conditions, one of the pores appearing in the system sees itself on the opposite edge of the simulated box. This leads to a sort of fusion of the pore with itself, resulting to an overall hole going across the whole length of the box. As a consequence, the lamellar phase cannot surround this presence, acquiring an additional restriction to its motions.

This behaviour reflects the trend of the derived rotational autocorrelation functions over time from the simulated trajectories of the C-H bonds: referring to eq. 4.1, the calculated $g(\tau)$ are shown for different sites of the molecule. The overall trend of the correlation functions over time reflects the expected decay of the fast-motional regimes, going from one at time zero to a plateau value with the increasing of the time. Furthemore, the distinct motional scales distinguishing the different portions of the molecule are confirmed by the different rate of the described decays: a comparison between from Fig. 5.8a - 5.8b - 5.8c shows a faster decay for the very external sites of the molecule, getting slower by going towards the central portion of it.

Still, the reproduced decay fails with regards to the plateau value reached by the

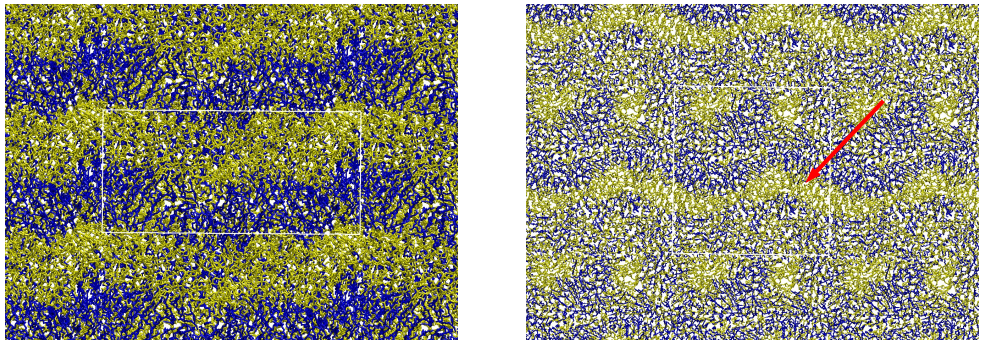

(a) (b)

Figure 5.5: Snapshots taken from MD simulation of the system composed by the surfactant in lamellar phase (blue) and water (yellow) from the lateral (Left) and top (Right) perspective. The white square delimitates the simulated box from the periodic image construction. The red arrow points at the elongated pore predicted by the simulations.

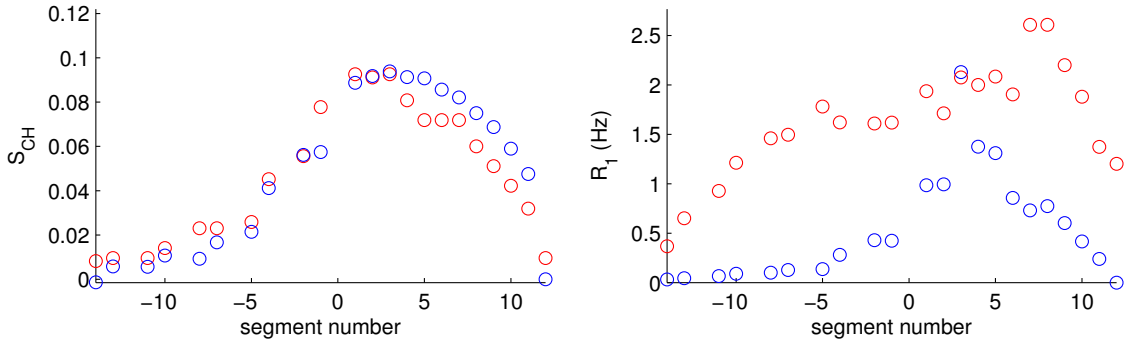

Figure 5.6: NMR experimental (red) and MD simulation (blue) values of S^2_{CH} order parameter (trhough eq. 3.4 from the experiments and eq. 4.2 from the simulations) and R_1 relaxation rate (through eq. 3.3 from the experiments and eq. 2.22 from the simulations) for the different ^{13}C sites in $C_{12}E_5/D_2O$ (lamellar phase with 77 wt% of surfactant, T=300° K and ω_1=25.9 KHz).

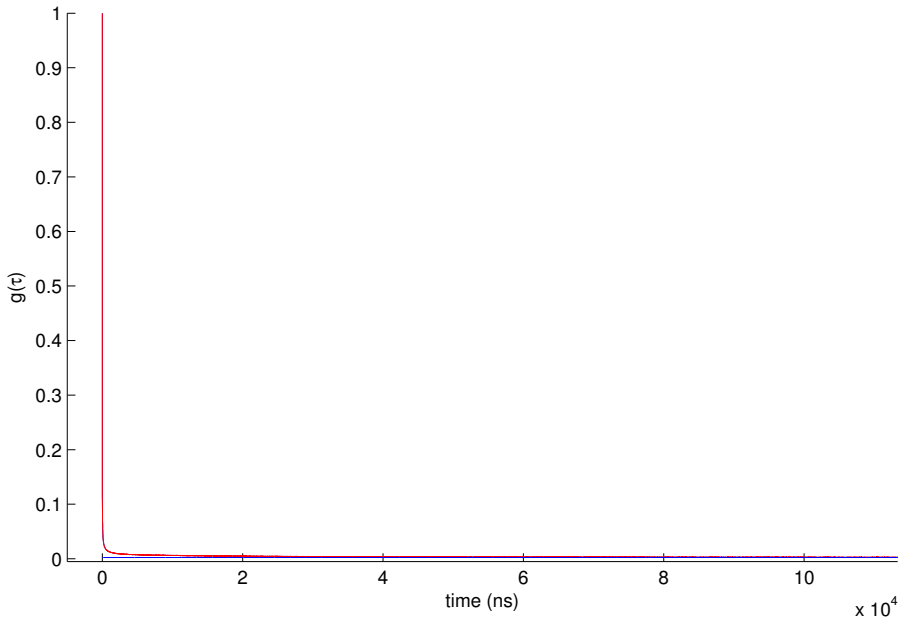

Figure 5.7: Decay over time of the correlation function calculated from the simulations (eq. 4.1) referring to the C-H bonds of carbon number 11. In blue the expected plateau corresponding to the value of S^2_{CH} (eq. 4.2) is plotted.

correlation functions, that does not correspond to the value of the order parameter squared, but tends to be lower if not even negative. This disagreement with the model presented in this work lowers the reliability of the further derivations and the consistence of the comparisons with the experimental results.

The effective correlation time evaluated by integrating the correlation function (eq. 4.3) is compared with the values obtained through the NMR derivations, and in better agreement regarding the tail portion of the surfactant (Fig. 5.9). The evaluation of the spectral density $j(\omega)$ from eq. 4.10 is then achieved, leading to the derivation of the R_1 rate constant through eq. 2.22 and again of the effective correlation time, this time through the value of $j(\omega)$ at the experimental nutation frequency (eq. 2.21). The results are shown in Fig. 5.6 and Fig. 5.9, and the agreement with the values obtained through the NMR procedue appears lowered. The main explanation is thought to be due to the decay of the simulated correlation functions, that does not fit in the descrpition of this model.

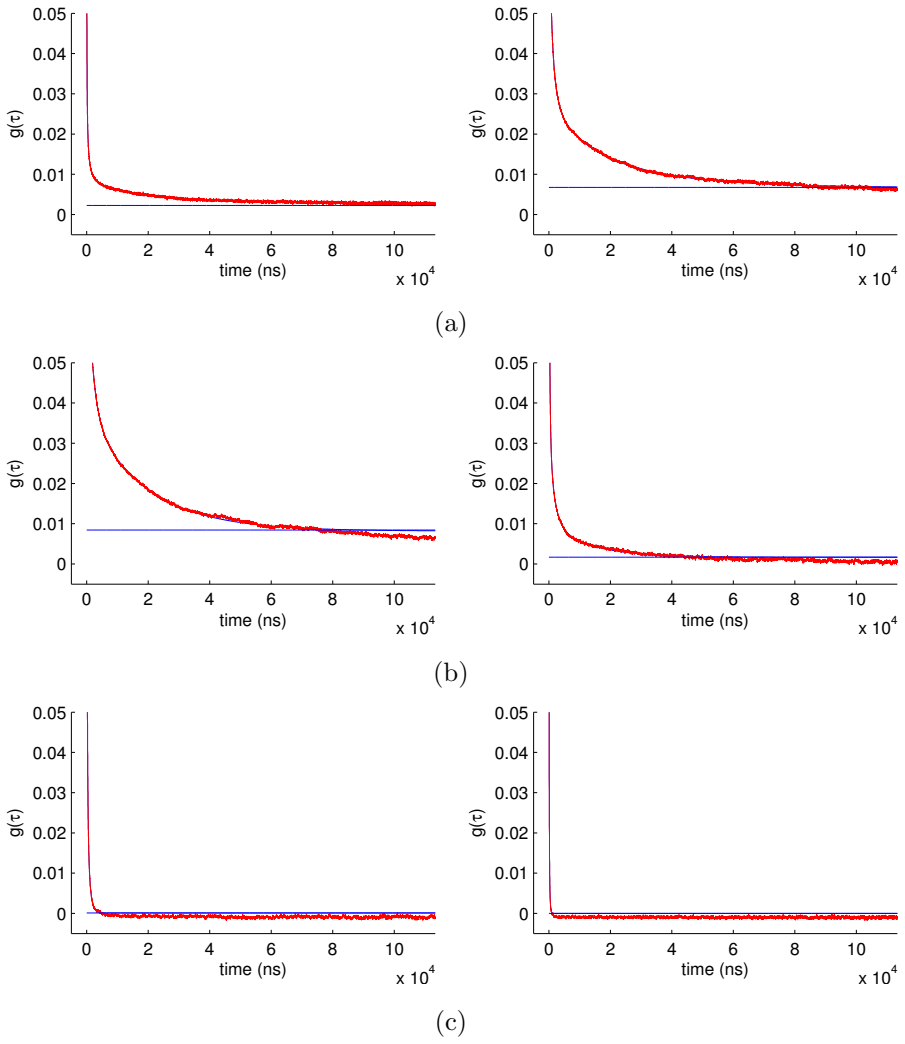

Figure 5.8: Decay over time of the correlation functions calculated from the simulations (eq. 4.1) referring to the C-H bonds of carbons number: 11 (Left) and 7 (Right) (Fig. 5.8a); 2 (Left) and -4 (Right) (Fig. 5.8b); -10 (Left) and -14 (Right) (Fig. 5.8c). In blue the expected plateau corresponding to the value of S^2_{CH} (eq. 4.2) is plotted.

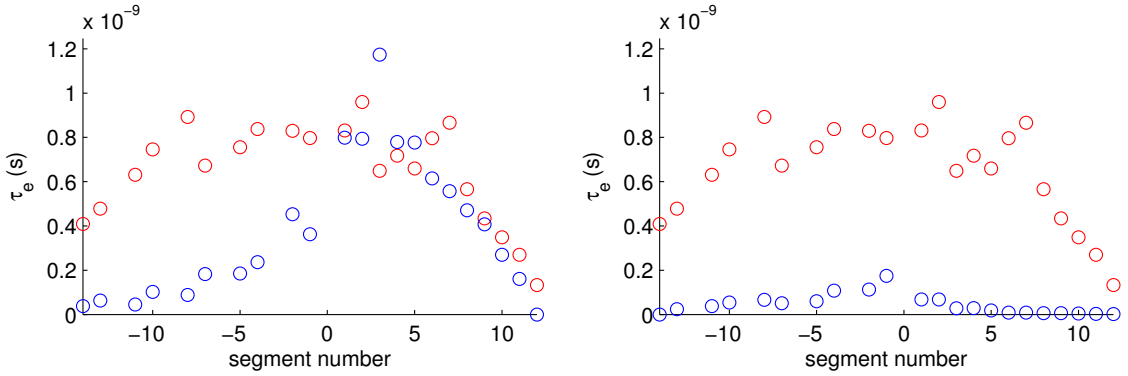

Figure 5.9: Values of τ_e obtained from the NMR experiments through eq. 2.24 (red) and from the MD simulation through eq. 4.3 (blue - Left) and eq. 2.21 (blue - Right) for the different ^{13}C sites in $C_{12}E_5/D_2O$ (lamellar phase with 77 wt% of surfactant, T=300° K and ω_1=25.9 KHz).

Chapter 6

Conclusions

With this work, a theoretical framework for interpreting and studying the motional processes occurring in a surfactant in lamellar phase is presented. The specific form of the correlation function describing the motions of the C-H bond is shown: it reveals two main decays of $g(\tau)$ due to the fast and slow motions inside the phase, among which the correlation function describes a plateau range corresponding to $g(\tau)=S^2_{CH}$. This particular dependence of $g(\tau)$ on time allows the evaluation of the effective correlation time characterising the fast motions inside the molecule, directly derivable from the area described by the correlation function from time zero to the reach of the plateau.

The results confirm the expected time-scale of these fast motions to be of the order of 10^{-10} s; furthemore, a faster dynamics appears to predominate in the external portions of the molecule, assiociated with a τ_e of one order of magnitude lower than the values characterizing the fast motions of the central part.

^{13}C NMR techinique demonstrates to be an efficient and complete source of analysis, providing the information needed for the study in all its steps. An efficient test for the accuracy of the obtained results is achievable through MD simulations, that allow to obtaine a detailed insight on the internal motions occurring in the surfactant at fast timescales.

Chapter 7

Acknowledgement

I would like to thank Daniel Topgaard for the chance he gave me of joining his group, and Samuli and Tiago for their guidance and patience. Special thanks to Tiago for the reliefs and the way he handled with my lack of self-confidence.
I would like to thank also my Family, my Big Family and all the friends I met in Lund for helping me to take all this easy.

Above all, greatest thanks to the two men of my Swedish life, Daniele and João, for being so nice and beautiful. After all, going through this with you, guys, had been just awesome. (:

Bibliography

[1] S. Yip, *Handbook of materials modeling*. Springer, 2005.

[2] M. Brown, A. Ribeiro, and G. Williams, "New view of lipid bilayer dynamics from 2h and 13c nmr relaxation time measurements," *Proceedings of the National Academy of Sciences*, vol. 80, no. 14, pp. 4325–4329, 1983.

[3] W. Schnepp and C. Schmidt, "Conformational order of amphiphilic chain molecules in lyotropic liquid-crystalline phases," *Berichte der Bunsengesellschaft für physikalische Chemie*, vol. 98, no. 2, pp. 248–252, 2010.

[4] H. Petrache, K. Tu, and J. Nagle, "Analysis of simulated nmr order parameters for lipid bilayer structure determination," *Biophysical journal*, vol. 76, no. 5, pp. 2479–2487, 1999.

[5] J. Peng and G. Wagner, "Mapping of spectral density functions using heteronuclear nmr relaxation measurements," 1992.

[6] J. Cohen, "Magnetic resonance in biology," 1983.

[7] F. Auguste, J. Douliez, A. Bellocq, E. Dufourc, and T. Gulik-Krzywicki, "Evidence for multilamellar vesicles in the lamellar phase of an electrostatic lyotropic ternary system. a solid state 2h-nmr and freeze fracture electron microscopy study," *Langmuir*, vol. 13, no. 4, pp. 666–672, 1997.

[8] W. Schnepp, S. Disch, and C. Schmidt, "2h nmr study on the lyomesophases of the system hexaethylene glycol dodecyl methyl ether/water temperature dependence of quadrupole splittings," *Liquid Crystals*, vol. 14, no. 3, pp. 843–852, 1993.

[9] M. Lukaschek, S. Müller, A. Hasennindl, C. Schmidt, and D. Grabowski, "Lamellar lyomesophases under shear as studied by deuterium nuclear magnetic resonance," *Colloid & Polymer Science*, vol. 274, no. 1, pp. 1–7, 1996.

[10] C. Fairhurst, M. Holmes, and M. Leaver, "Structure and morphology of the intermediate phase region in the nonionic surfactant c16eo6/water system," *Langmuir*, vol. 13, no. 19, pp. 4964–4975, 1997.

[11] M. Baciu, U. Olsson, M. Leaver, and M. Holmes, "2h nmr evidence for the formation of random mesh phases in nonionic surfactant-water systems," *The Journal of Physical Chemistry B*, vol. 110, no. 16, pp. 8184–8187, 2006.

[12] A. Tonegawa, K. Ohno, H. Matsuura, K. Yamada, and T. Okuda, "A combined raman and deuterium nmr spectroscopic study on the molecular and phase structure of a nonionic surfactant c12e5-water system," *The Journal of Physical Chemistry B*, vol. 106, no. 51, pp. 13211–13223, 2002.

[13] H. Petrache, S. Dodd, and M. Brown, "Area per lipid and acyl length distributions in fluid phosphatidylcholines determined by (2) h nmr spectroscopy.," *Biophysical journal*, vol. 79, no. 6, p. 3172, 2000.

[14] C. Le Guerneve and M. Auger, "New approach to study fast and slow motions in lipid bilayers: application to dimyristoylphosphatidylcholine-cholesterol interactions," *Biophysical journal*, vol. 68, no. 5, pp. 1952–1959, 1995.

[15] G. Lipari and A. Szabo, "Model-free approach to the interpretation of nuclear magnetic resonance relaxation in macromolecules. 1. theory and range of validity," *Journal of the American Chemical Society*, vol. 104, no. 17, pp. 4546–4559, 1982.

[16] A. Nowacka, P. Mohr, J. Norrman, R. Martin, and D. Topgaard, "Polarization transfer solid-state nmr for studying surfactant phase behavior," *Langmuir*, vol. 26, no. 22, pp. 16848–16856, 2010.

[17] A. Nowacka, S. Douezan, L. Wadsö, D. Topgaard, and E. Sparr, "Small polar molecules like glycerol and urea can preserve the fluidity of lipid bilayers under dry conditions," *Soft Matter*, vol. 8, no. 5, pp. 1482–1491, 2012.

[18] M. Levitt, *Spin dynamics*. Wiley Chichester, UK, 2001.

[19] J. Keeler, *Understanding NMR spectroscopy*. John Wiley & Sons, 2011.

[20] D. Laws, H. Bitter, and A. Jerschow, "Solid-state nmr spectroscopic methods in chemistry," *Angewandte Chemie International Edition*, vol. 41, no. 17, pp. 3096–3129, 2002.

[21] J. Hirschinger, "A simple analytical model to describe dynamic magic-angle spinning experiments," *Concepts in Magnetic Resonance Part A*, vol. 28, no. 5, pp. 307–320, 2006.

[22] A. Zayed, "A convolution and product theorem for the fractional fourier transform," *Signal Processing Letters, IEEE*, vol. 5, no. 4, pp. 101–103, 1998.

[23] R. Harris, *Nuclear magnetic resonance*, vol. 3. Royal Society of Chemistry, 1974.

[24] A. Abragam, *Principles of nuclear magnetism*, vol. 32. Oxford University Press, USA, 1983.

[25] S. Feller, "Molecular dynamics simulations of lipid bilayers," *Current opinion in colloid & interface science*, vol. 5, no. 3, pp. 217–223, 2000.

[26] S. Feller, D. Yin, R. Pastor, and A. MacKerell, "Molecular dynamics simulation of unsaturated lipid bilayers at low hydration: parameterization and comparison with diffraction studies," *Biophysical journal*, vol. 73, no. 5, pp. 2269–2279, 1997.

[27] T. Ferreira, B. Medronho, R. Martin, and D. Topgaard, "Segmental order parameters in a nonionic surfactant lamellar phase studied with 1h–13c solid-state nmr," *Phys. Chem. Chem. Phys.*, vol. 10, no. 39, pp. 6033–6038, 2008.

[28] M. Imai, A. Saeki, T. Teramoto, A. Kawaguchi, K. Nakaya, T. Kato, and K. Ito, "Kinetic pathway of lamellar: gyroid transition: Pretransition and transient states," *The Journal of Chemical Physics*, vol. 115, p. 10525, 2001.

[29] G. Morris and R. Freeman, "Enhancement of nuclear magnetic resonance signals by polarization transfer," *Journal of the American Chemical Society*, vol. 101, no. 3, pp. 760–762, 1979.

[30] J. Gross, P. Costa, J. Dubacq, D. Warschawski, P. Lirsac, P. Devaux, and R. Griffin, "Multidimensional nmr in lipid systems. coherence transfer through j couplings under mas," *Journal of Magnetic Resonance, Series B*, vol. 106, no. 2, pp. 187–190, 1995.

[31] S. Dvinskikh, H. Zimmermann, A. Maliniak, and D. Sandström, "Measurements of motionally averaged heteronuclear dipolar couplings in mas nmr using r-type recoupling," *Journal of Magnetic Resonance*, vol. 168, no. 2, pp. 194–201, 2004.

[32] X. Zhao, M. Edén, and M. Levitt, "Recoupling of heteronuclear dipolar interactions in solid-state nmr using symmetry-based pulse sequences," *Chemical physics letters*, vol. 342, no. 3, pp. 353–361, 2001.

[33] M. Hong, A. Pines, and S. Caldarelli, "Measurement and assignment of long-range ch dipolar couplings in liquid crystals by two-dimensional nmr spectroscopy," *The Journal of Physical Chemistry*, vol. 100, no. 35, pp. 14815–14822, 1996.

[34] MATLAB, *version 7.10.0 (R2010a)*. Natick, Massachusetts: The MathWorks Inc., 2010.

[35] D. Van Der Spoel, E. Lindahl, B. Hess, G. Groenhof, A. Mark, and H. Berendsen, "Gromacs: fast, flexible, and free," *Journal of computational chemistry*, vol. 26, no. 16, pp. 1701–1718, 2005.

[36] W. van Gunsteren, S. Billeter, A. Eising, P. Hünenberger, P. Krüger, A. Mark, W. Scott, and I. Tironi, "Biomolecular simulation: The {GROMOS96} manual and user guide," 1996.

[37] L. Schuler, X. Daura, and W. Van Gunsteren, "An improved gromos96 force field for aliphatic hydrocarbons in the condensed phase," *Journal of Computational Chemistry*, vol. 22, no. 11, pp. 1205–1218, 2001.

[38] J. Briggs, T. Matsui, and W. Jorgensen, "Monte carlo simulations of liquid alkyl ethers with the opls potential functions," *Journal of Computational Chemistry*, vol. 11, no. 8, pp. 958–971, 1990.

[39] B. Shang, Z. Wang, and R. Larson, "Molecular dynamics simulation of interactions between a sodium dodecyl sulfate micelle and a poly (ethylene oxide) polymer," *The Journal of Physical Chemistry B*, vol. 112, no. 10, pp. 2888–2900, 2008.

[40] H. Berendsen, J. Postma, W. Van Gunsteren, J. Hermans, *et al.*, "Interaction models for water in relation to protein hydration," *Intermolecular forces*, vol. 11, pp. 331–342, 1981.

[41] S. Nose and M. Klein, "Constant pressure molecular dynamics for molecular systems," *Molecular Physics*, vol. 50, no. 5, pp. 1055–1076, 1983.

[42] M. Parrinello and A. Rahman, "Polymorphic transitions in single crystals: A new molecular dynamics method," *Journal of Applied physics*, vol. 52, no. 12, pp. 7182–7190, 1981.

[43] D. Evans and B. Holian, "The nose–hoover thermostat," *The Journal of chemical physics*, vol. 83, p. 4069, 1985.

[44] E. Ulrich, P. Lalith, L. Max, D. Tom, L. Hsing, and G. Lee, "A smooth particle mesh ewald method," *J Chem Phys*, vol. 103, pp. 8577–8593, 1995.

[45] B. Hess, H. Bekker, H. Berendsen, and J. Fraaije, "Lincs: a linear constraint solver for molecular simulations," *Journal of computational chemistry*, vol. 18, no. 12, pp. 1463–1472, 1997.

[46] S. Miyamoto and P. Kollman, "Settle: an analytical version of the shake and rattle algorithm for rigid water models," *Journal of computational chemistry*, vol. 13, no. 8, pp. 952–962, 1992.

[47] T. Ahlnäs, G. Karlström, and B. Lindman, "Dynamics and order of nonionic surfactants in neat liquid and micellar solution from multifield carbon-13 nmr relaxation and carbon-13 nmr chemical shifts," *Journal of Physical Chemistry*, vol. 91, no. 15, pp. 4030–4036, 1987.

[48] H. Wennerstroem, B. Lindman, O. Soederman, T. Drakenberg, and J. Rosenholm, "Carbon-13 magnetic relaxation in micellar solutions. influence of aggregate motion on t1," *Journal of the American Chemical Society*, vol. 101, no. 23, pp. 6860–6864, 1979.

[49] G. Karlstroem, "A new model for upper and lower critical solution temperatures in poly (ethylene oxide) solutions," *The Journal of Physical Chemistry*, vol. 89, no. 23, pp. 4962–4964, 1985.